ECCOMAS Congress 2016
VII European Congress on Computational Methods in Applied Sciences and Engineering
M. Papadrakakis, V. Papadopoulos, G. Stefanou, V. Plevris (eds.)
Crete Island, Greece, 5–10 June 2016

STRUCTURAL ANALYSIS OF ADHESIVE BONDING FOR THICK-WALLED TUBULAR COMPOSITE PROFILES

Geminiano Mancusi[1], Agostina Orefice[1], Luciano Feo[1], Fernando Fraternali[1]

[1] Department of Civil Engineering, University of Salerno
Via Giovanni Paolo II 132, 84084 Fisciano (SA), Italy
e-mail: {g.mancusi,aorefice,l.feo,f.fraternali}@unisa.it

Keywords: Tubular profiles, GFRP, Space frame truss, Adhesive bonding.

Abstract A *mechanical model for predicting the response of a GFRP tubular truss member glued to terminal* (*nodal*) *devices is presented. The given model captures shear deformation and simulates adhesion between the composite tube and the nodal devices via an appropriate cohesive interface. A comparison between theoretical and experimental results highlights a very good theory-experiment matching in terms of failure load and global displacements.*

1. INTRODUCTION

Thick-walled tubular composite profiles with annular cross-section represent the optimal solution for 3-D large space frame trusses.

Within this context, glass fibre-reinforced polymers (GFRPs) are usually considered, due to the best match between expected costs and benefits, in combination with adhesive bonding solutions [1-4] between the composite member and standard co-axial nodal devices, generally made of stainless stell parts (Fig. 1).

Figure 1: Example of nodal device (spherical hinge).

Although internal stresses essentially accord to the axial regime, shear stresses originated by the interfacial interactions over the adhesive bonding zones can be present within the composite tube. As a consequence, the local behaviour of the composite profile is affected by shear stresses and, of course, the failure criterion should account for this aspect.

Considering the usually low values of shear moduli for GFRP, there is a great interest in investigating the complex interplay between I/II interfacial failure modes [5-7] and local shear deformations [8-10] which occur within the thickness of the composite member.

In this view, a mechanical model based on an appropriate kinematics has been proposed in combination with a mixed mode cohesive failure criterion. The aim is to predict both the structural response at the service conditions and the ultimate strength of the joint, thus allowing a refined structural analysis of the whole structure accounting for the local shear strains too.

In Figure 2 the equilibrium problem under discussion is exemplified with respect to a single composite tube bonded to apposite hinge nodal devices able to guarantee the internal connections among many parts of a generic space frame truss. Orthonormal unit vectors $\mathbf{i}_1$, $\mathbf{i}_2$ and $\mathbf{k}$ are introduced, with $\mathbf{k}$ aligned to the z-axis, as well as the point $\mathbf{O}$ as an origin. An axisymmetric normal stress distribution $p_z(r)$ is considered over the end cross-sections of the system, being r the radial coordinate, as indicated in the following.

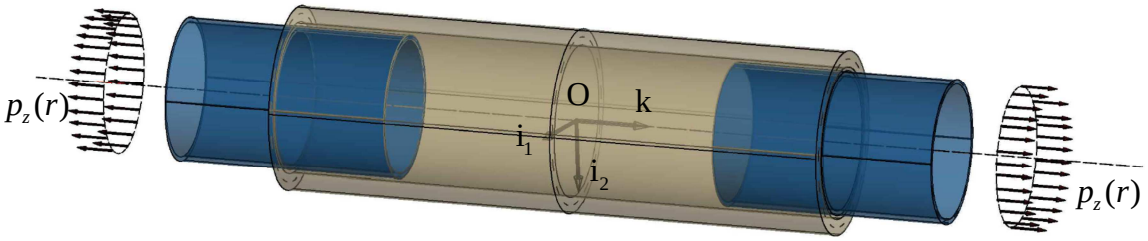

Figure 2: Equilibrium problem under consideration.

2. THE MECHANICAL MODEL

The mechanical model proposed for studying the adhesive bonding of tubular profiles is based on appropriate kinematic hypotheses, briefly summarised in the Appendix.

Three coaxial elements are considered: the GFRP annular pultruded profile and the nodal devices bonded at the ends of the tube. Symbols are as indicated in Figs. 3.a-b.

Orthotropic stress-strain relationships with transverse isotropy are chosen to simulate the constitutive response of the composite (see Appendix), while isotropic equations are used for what concerns the constitutive behaviour of the stainless steel.

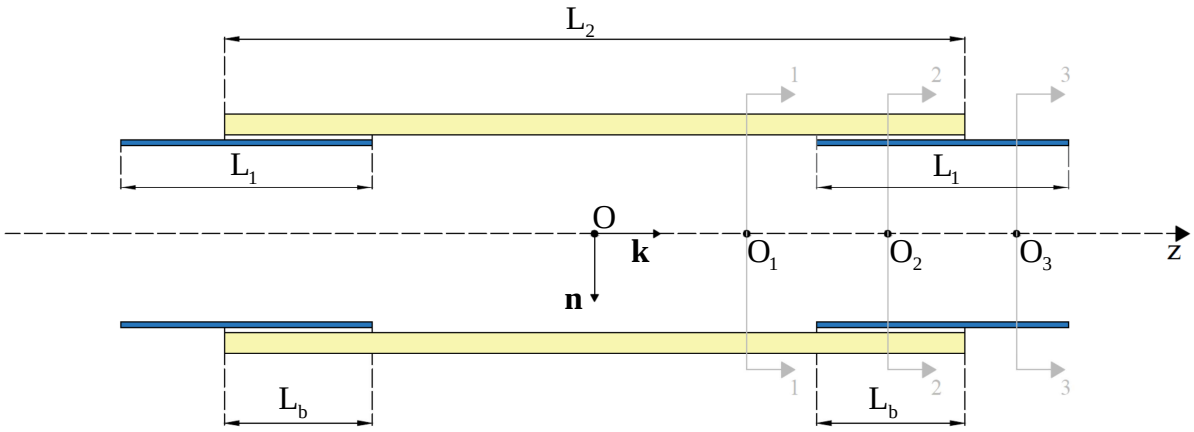

Figure 3.a : Geometric configuration (longitudinal section).

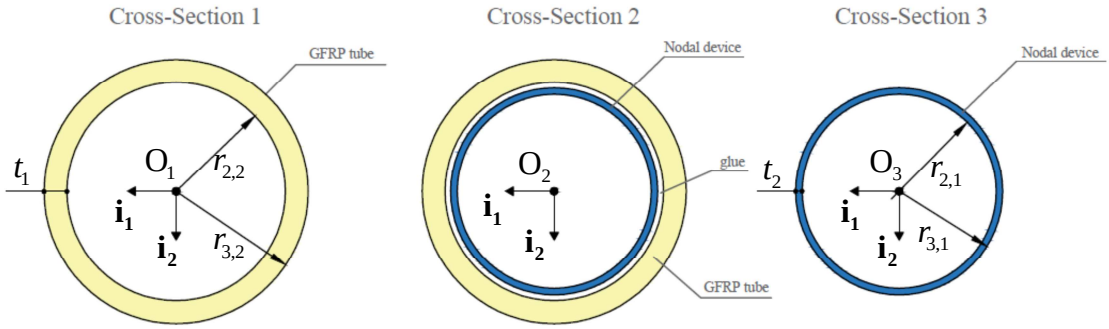

Figure 3.b : Geometric configuration (relevant cross-sections).

Due to axisymmetric condition, the adhesive bonding is modelled by a 2-D continuous distribution of cohesive forces acting over the bonding interfaces along both the normal ($\mathbf{n}$, radial) and the tangential ($\mathbf{k}$, axial) directions; these forces work to contrast the interfacial displacements between the composite tube and the nodal devices. The following additional symbols are introduced with this regard: d_r and t_{rr} denoting the interfacial normal displacement (i.e. discontinuous) and the interfacial normal traction (per unit surface) as well as d_k and t_{rk} indicating the analogous quantities with respect to the axial direction (Fig. 4).

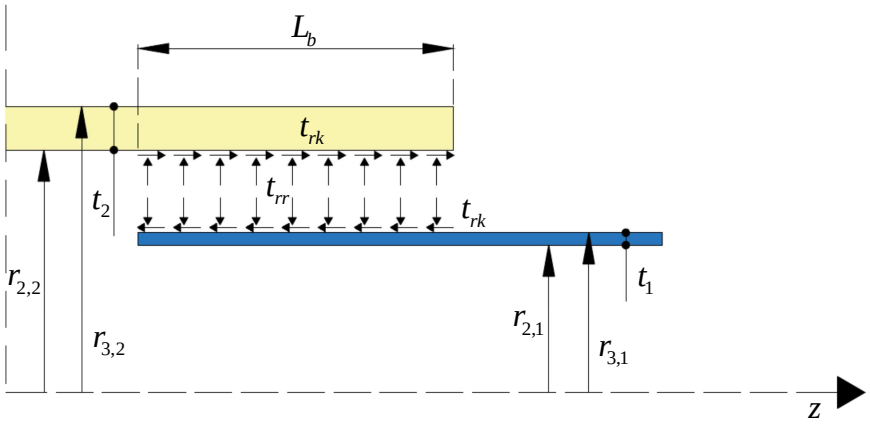

Figure 4 : Interfacial cohesive forces t_{rr} and t_{rk} (per unit surface).

An exponential cohesive interface model has been derived from that one proposed in [11-12] in order to include possible coupling between normal and tangential discontinuous displacements. The following potential has been considered:

$$F(h) = \Phi_U \left[1 - \left(1 + \frac{h}{h_c} \right) e^{-(h/h_c)} \right] \tag{1}$$

In eqn. (1) the symbol h indicates the norm of the vector $\mathbf{h}$:

$$\mathbf{h} = \lambda_I \, d_r \, \mathbf{n} + \lambda_{II} \, d_k \, \mathbf{k} \tag{2}$$

with λ_I and λ_{II} accounting for the coupling between the normal and tangential interfacial displacements. The corresponding interaction, $\mathbf{p}$, is assumed as follows:

$$\mathbf{p} = \frac{1}{\lambda_I} t_{rr} \, \mathbf{n} + \frac{1}{\lambda_{II}} t_{rk} \, \mathbf{k} = p \frac{\mathbf{h}}{h} \tag{3}$$

where:

$$p = \frac{dF}{dh} = p_c \frac{h}{h_c} e^{(1-h/h_c)} \tag{4}$$

The quantities h_c and p_c are parameters of the interface model, while Φ_U represents the fracture energy per unit surface. It results:

$$h = \sqrt{(\lambda_I \, d_r)^2 + (\lambda_{II} \, d_k)^2} \qquad p = \sqrt{\left(\frac{t_{rr}}{\lambda_I} \right)^2 + \left(\frac{t_{rk}}{\lambda_{II}} \right)^2} \qquad \Phi_U = e \, p_c \, h_c \tag{5.a-c}$$

The cohesive model simulates the softening effect for $h > h_c$. Moreover, from a rigorous point of view, the full degradation is only asymptotic (for $h \to \infty$).

3. NUMERICAL ANALYSES

The mechanical model presented in the previous Section 2 has been approximated via a finite element technique in order to provide many numerical results of major relevance concerning the behaviour of a tubular composite profile bonded at the ends to apposite nodal devices.

The equilibrium problem indicated in Fig. 2 has been approached numerically by means of a finite element approximation. The mesh proposed is composed of 2 node finite elements characterized by 24 degrees of freedom, including 12 d.o.f. per each node.

According to the discussion summarized in the Appendix, let $w_{i,j}(z)$ be the axial displacement field of the j-part at $r = r_i$ (with j=1 indicating the nodal device while j=2 denoting the GFRP tube). The approximation of $w_{i,j}$ is obtained by cubic interpolating polynomials as follows:

$$w_{i,j}(\zeta) = \mathrm{h}_{10}(\zeta)\, w_{i,j}^{(1)} + \mathrm{h}_{11}(\zeta)\, w_{i,j}'^{(1)} + \mathrm{h}_{20}(\zeta)\, w_{i,j}^{(2)} + \mathrm{h}_{21}(\zeta)\, w_{i,j}'^{(2)} \tag{6}$$

where:

$$\mathrm{h}_{10} = \frac{1}{4}\left(2 - 3\zeta + \zeta^3\right) \qquad \mathrm{h}_{11} = \frac{l_\mathrm{e}}{8}\left(1 - \zeta - \zeta^2 + \zeta^3\right) \tag{7.a-b}$$

$$\mathrm{h}_{20} = \frac{1}{4}\left(2 + 3\zeta - \zeta^3\right) \qquad \mathrm{h}_{21} = \frac{l_\mathrm{e}}{8}\left(-1 - \zeta + \zeta^2 + \zeta^3\right) \tag{7.c-d}$$

being l_e the length of the finite element; $w_{i,j}^{(1)}$ and $w_{i,j}^{(2)}$ the nodal values of the kinematic unknown under consideration while $w_{i,j}'^{(1)}$ and $w_{i,j}'^{(2)}$ the nodal values of the derivative of $w_{i,j}$ with respect to the axial coordinate z.

Using standard notations, the following generalized displacements vector $\mathbf{w}_{(e)}$, with dimensions 6×1, is introduced as a function of the nodal unknowns $\mathbf{U}_{(e)}$ over the generic finite element:

$$\mathbf{w}_{(e)} = \left[\left(w_{1,1}, w_{2,1}, w_{3,1}\right), \left(w_{1,2}, w_{2,2}, w_{3,2}\right)\right]^T = \mathbf{N}\mathbf{U}_{(e)} \tag{8}$$

In eqn. (8) the symbol $\mathbf{N}$ denotes the following four-block matrix, with dimensions 6×24:

$$\mathbf{N} = \left[\mathbf{N}_{10}, \mathbf{N}_{11}, \mathbf{N}_{20}, \mathbf{N}_{21}\right] \tag{9}$$

where:

$$\mathbf{N}_{\mathrm{pq}} = \mathrm{diag}\left(\mathrm{h}_{\mathrm{pq}}, \mathrm{h}_{\mathrm{pq}}, \mathrm{h}_{\mathrm{pq}}, \mathrm{h}_{\mathrm{pq}}, \mathrm{h}_{\mathrm{pq}}, \mathrm{h}_{\mathrm{pq}}\right) \quad \text{(p=1, 2 and q=0, 1)} \tag{10}$$

Furthermore, $\mathbf{U}_{(e)}$ is a numeric vector, with dimensions 24×1, which collects the values of the kinematic unknowns attained at both the nodes of the finite element:

$$\mathbf{U}_{(e)} = \left[\mathbf{U}_{(e,1)}^T, \mathbf{U}_{(e,2)}^T\right]^T \tag{11}$$

with $\mathbf{U}_{(e,n)}$ denoting the kinematic unknowns at the n node (n=1, 2):

$$\mathbf{U}_{(e,n)} = \left[\left(w_{1,1}^{(n)}, w_{2,1}^{(n)}, w_{3,1}^{(n)}, w_{1,2}^{(n)}, w_{2,2}^{(n)}, w_{3,2}^{(n)} \right), \left(w_{1,1}^{\prime(n)}, w_{2,1}^{\prime(n)}, w_{3,1}^{\prime(n)}, w_{1,2}^{\prime(n)}, w_{2,2}^{\prime(n)}, w_{3,2}^{\prime(n)} \right) \right]^T \qquad (12)$$

In Figure 5 the whole list of the nodal unknowns is identified.

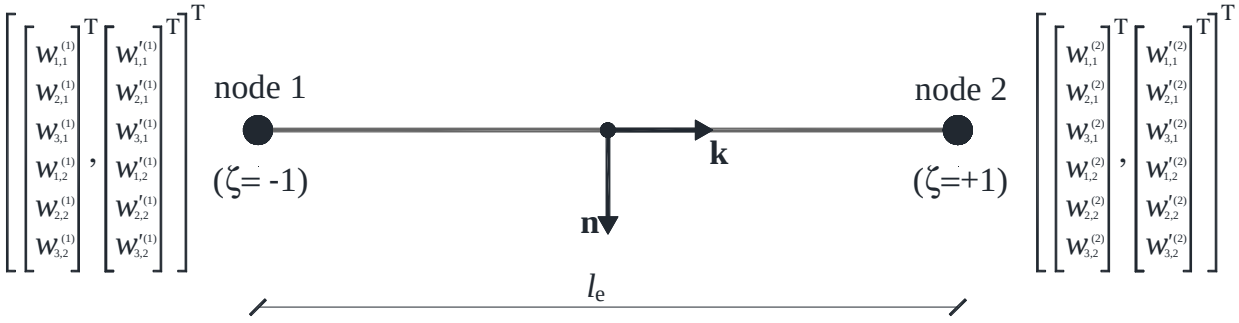

Figure 5 : Finite element.

A more accurate discussion deals with the approximation of the non-linear interfacial interactions. With reference to the generic finite element, the interfacial displacements along both the n-axis and the z-axis, d_r and d_k, can be expressed as a function of the nodal unknowns $\mathbf{U}_{(e)}$. If Mode II only is present ($d_r = 0$), then $\mathbf{h} = \lambda_{II}\, d_k\, \mathbf{k}$. Under this assumption, the interfacial behaviour is represented by a unique cohesive relationship between t_{rk} and d_k. It results:

$$d_k = \mathbf{DNU}_{(e)} \qquad (13)$$

with $\mathbf{D}$ the following numeric vector, with dimensions 1×6:

$$\mathbf{D} = [0, 0, -1, 0, 1, 0] \qquad (14)$$

Moreover, the interfacial interaction along the z-axis, t_{rk}, is:

$$t_{rk} = \kappa d_k \qquad (15)$$

where the symbol κ denotes the secant slope of the cohesive law:

$$\kappa = \lambda_{II} \frac{p_c}{h_c} e^{(1-\lambda_{II} d_k / h_c)} \qquad (16)$$

A standard iterative procedure can thereby be adopted for searching the numerical solution. The convergence of the numerical solution to the continuous solution is discussed in [13].

As a case study, a numerical simulation has been carried out in order to underline the power of the proposed model. The FE analysis deals with a configuration made of two stainless steel terminal devices bonded at the ends of a GFRP tube. The following geometric assumptions are considered.

inner radius of nodal device	($r_{2,1}$ = 59.5 mm)
outer radius of nodal device	($r_{3,1}$ = 63.5 mm)
thickness of nodal device wall	($t_1 = r_{3,1} - r_{2,1}$ = 4.0 mm)
inner radius of GFRP tube	($r_{2,2}$ = 66.0 mm)
outer radius of GFRP tube	($r_{3,2}$ = 80.0 mm)
thickness of GFRP tube wall	($t_2 = r_{3,2} - r_{2,2}$ = 14.0 mm)
length of the nodal device (coaxial part)	(L_1 =120.0 mm)
length of the GFRP tube	(L_2 = 500.0 mm)
length of the bonding zones	(L_b = 100.0 mm)
thickness of the glue layer	($t_a = r_{2,2} - r_{3,1}$ = 2.5 mm)

Table 1: Geometric properties.

transverse normal modulus	(E_T =3700 N/mm^2)
longitudinal normal modulus	(E_L =37000 N/mm^2)
shear modulus (**n** - **k** plane)	(G_{TL} =1850 N/mm^2)
Poisson coefficients	($\nu_{TT} = \nu_{TL} = \nu_{LT} = 0$)

Table 2: GFRP constitutive properties.

normal modulus	(E =196000 N/mm^2)
shear modulus	(G =98000 N/mm^2)
Poisson coefficient	($\nu = 0$)

Table 3: Stainless steel constitutive properties.

fracture energy (per unit surface)	($\Phi_U = 3.65 \times 10^{-2}$ Nmm/mm^2)
characteristic value of h	(h_c = 0.001 mm)
Mode I / Mode II interaction	($\lambda_I = \lambda_{II} = 1$)

Table 4: Parameters of the cohesive potential.

The loading condition considered is a resultant traction force equal to T=106000 N applied at the right end of the model, while the left end of the model is constrained to be fixed. From a mathematical point of view, the traction force has been simulated by means of two concentrated forces T/2 applied in a dual manner with respect to the following degrees of freedom, both relative to the steel device: $w_{2,1}$ and $w_{3,1}$. As discussed in [13], this is not rigorous in an absolute manner, but it can be acceptable for technical purposes when dealing with a moderately thick tubular wall. On the opposite end, the following degrees of freedom have been constrained to be equal to zero : $w_{1,1}$, $w_{2,1}$ and $w_{3,1}$.

The load intensity has been chosen in consideration that a preliminary experimental test has been recently performed, indicating the failure point of the bonded system exactly for T=106000 N, for a global elongation equal to 0.225 mm. Thereby, a numerical comparison in terms of interfacial energy absorption and global stiffness seems to be appropriate, in addition to a brief comment on the shear deformability of the composite tube.

The FE simulation has been carried out by means of a mesh composed of 540 finite elements with a constant length l_e =1.0 mm. The convergence finally achieved corresponds to a residual vector with a norm equal to 9.82×10^{-5}.

The following Figure 6.a-d show the effects of the shear strains as a function of r within the system at fixed values of the axial coordinate z. As it can be seen, these effects become relevant over the bonding zones ($z_I \le |z| \le z_{III}$ with $z_I = 150$ mm and $z_{III} = 250$ mm).

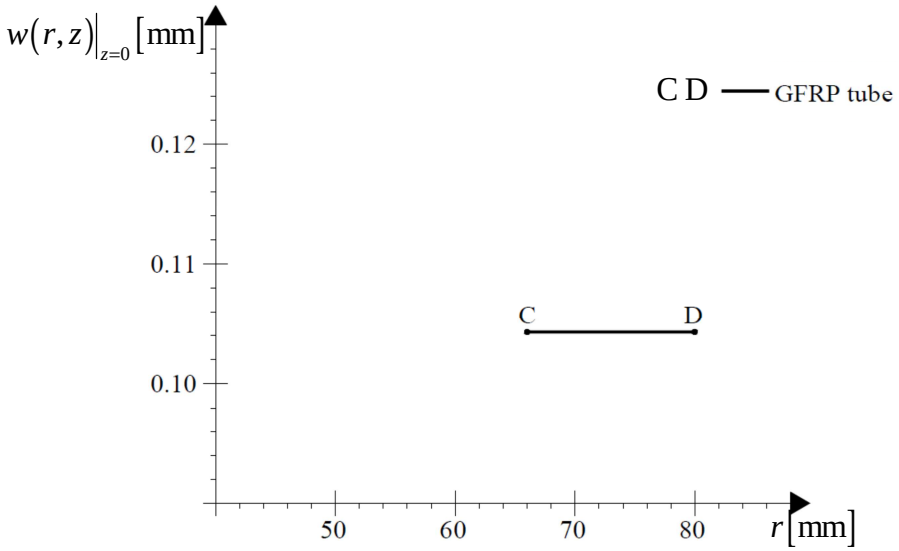

Figure 6.a : Axial displacement versus radial coordinate at $z = 0$ mm

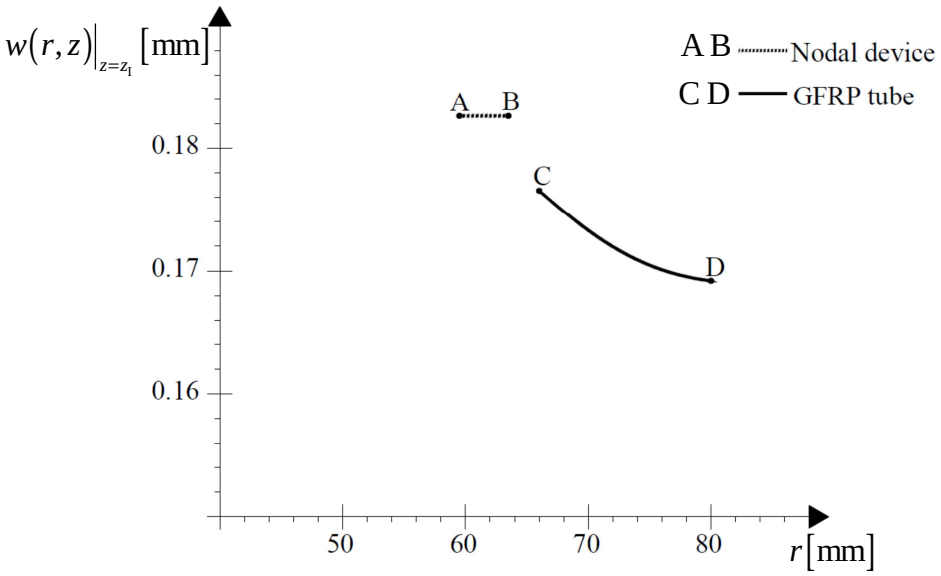

Figure 6.b : Axial displacement versus radial coordinate at $z = z_I = 150$ mm

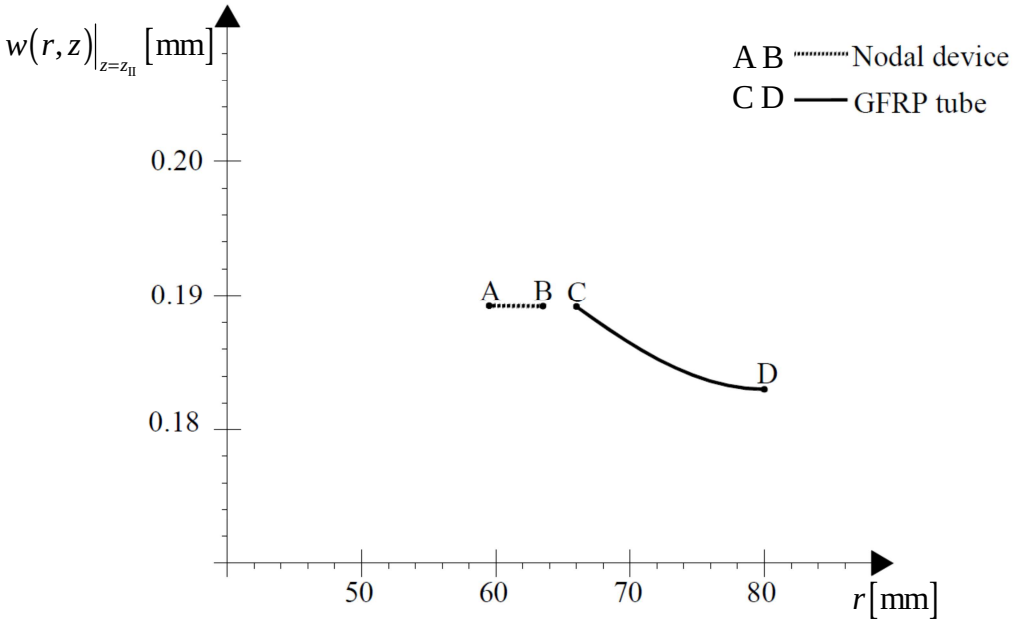

Figure 6.c : Axial displacement versus radial coordinate at $z = z_{II} = 200$ mm

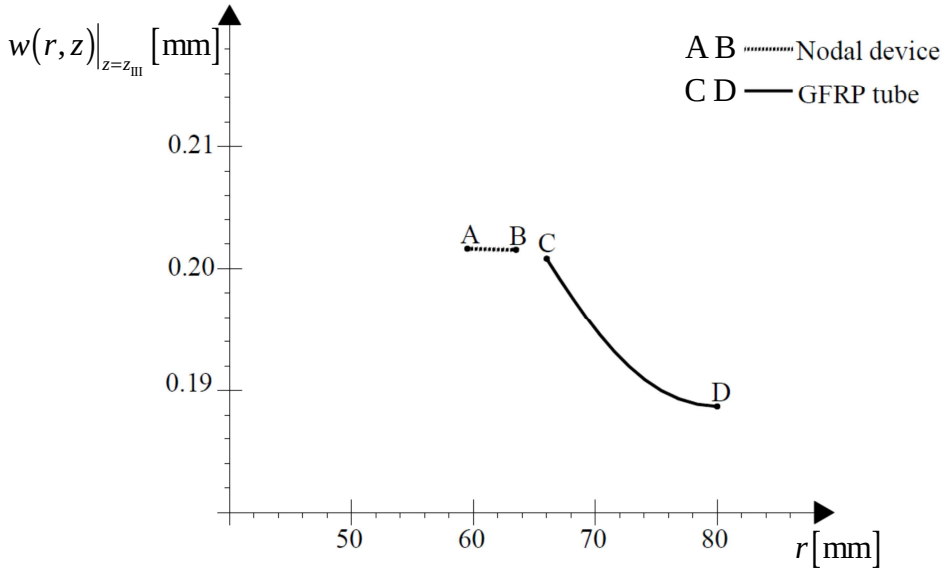

Figure 6.d : Axial displacement versus radial coordinate at $z = z_{III} = 250$ mm

In Figure 7, the interfacial cohesive force t_{rk} (per unit surface) has been plotted over the bonding length. Due to the symmetric behaviour of both the bonding zones, only the interface at the right end has been considered ($0 \le z^* \le L_b$ with $z^* = z - z_I$, $z_I = 150$ mm and $L_b = 100$ mm). The numerical analysis indicates that under the applied resultant traction force T=106000 N, the full degradation of the interface is substantially achieved at the axial coordinate $z_I = 150$ mm ($z^* = 0$ mm), as observed for the experimental test.

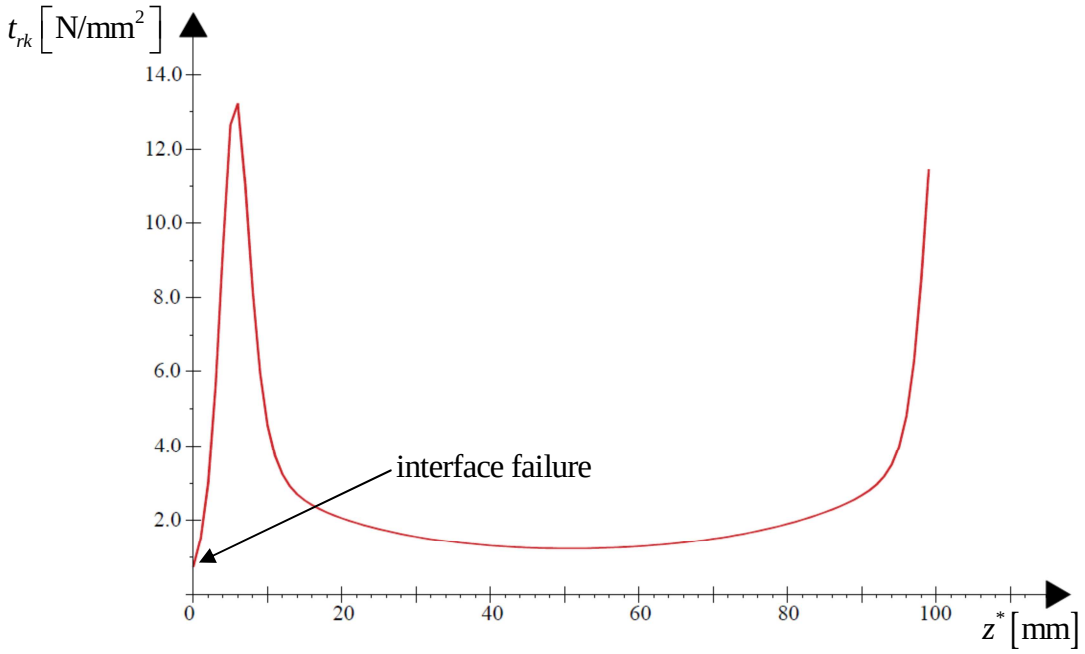

Figure 7: Interfacial cohesive forces t_{rk} (per unit length) versus $z^* = z - z_1$.

Finally, the numerical prediction of the global elongation of the system is equal to 0.209 mm, substantially the same that the experimental value (0.225 mm).

The previous example has been presented for the pure scope of highlighting the main features of the proposed model. Further developments will concern more sophisticated approach to the interface behaviour, on line with what is proposed in [14-16], as well as the optimization strategy with regard to the design of complex spatial bridge following recent trends as discussed in [17-19].

4. CONCLUDING REMARKS

In this paper the authors have presented a mechanical model for the 1-D study of a composite tubular profile loaded in traction/compression and bonded to coaxial terminal devices able to guarantee the connection of the member within a general structure. This problem is highly relevant in practice, considering the context of large space frame trusses, where the advantage in using GFRP members with annular cross-section is universally acknowledged.

The proposed formulation is based on a cohesive approach for the modeling of the interface as well as on appropriate assumptions for the kinematics of the composite member, which accounts for possible shear strains within the thickness of the tubular wall. This aspect assumes a relevant role in the structural analysis of the member from both a point of view concerning the accurate prediction of the global displacements and with reference to the local behavior of the tube. Over the bonding length, in fact, shear strains appear on the lateral surface of the tube as an effect of the interface cohesive interactions between the tube and the nodal device. As a consequence, the interface behavior is affected from shear deformability of the tubular profile as well as the failure load of the system.

5. APPENDIX – KINEMATICS OF ORTHOTROPIC COMPOSITE TUBES

5.1. Global reference frame

According to the global reference frame shown in Fig. 8, the position of a generic point **P** is given by:

$$\mathbf{x} = r\cos\vartheta\mathbf{i}_1 + r\sin\vartheta\mathbf{i}_2 + z\mathbf{k} \tag{A.1}$$

where r, ϑ and z are assumed as spatial variables. Due to axisymmetric geometry, the displacement field depends on r and z only. Moreover, the displacement field components are: u_r (radial), $u_\vartheta = 0$ (circumferential, null), w (axial).

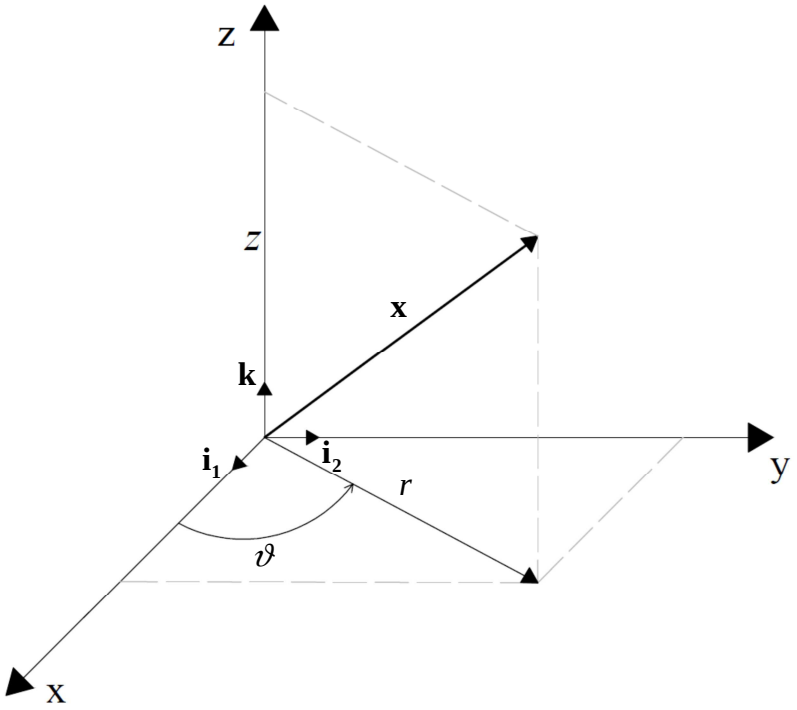

Figure 8 : Global reference frame.

5.2. Axial displacements

The axial displacement field is proposed in the following form:

$$w(r,z) = w_i(z)\, f_i(r) \quad (i = 1,\ 2,\ 3) \tag{A.2}$$

where $w_i(z)$ denotes the axial displacement field at a defined radial coordinate r_i, while $f_i(r)$ is a polynomial truncated at the second order terms.

The following assumptions are introduced:

$$r_1 = 0\,, \qquad r_2 = R_i\,, \qquad r_3 = R_e\,. \tag{A.3.a-c}$$

being R_i and R_e the inner and the outer radius of the annular cross-section (Fig.9).

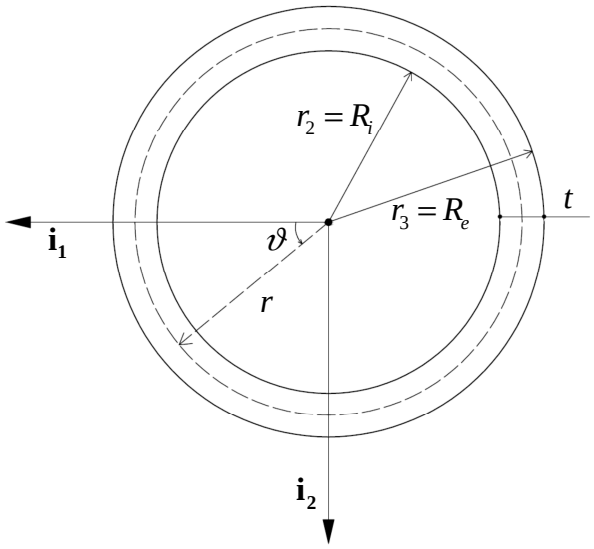

Figure 9 : Annular cross-section.

The polynomials $f_i(r)$ can be specified as indicated below:

$$f_1(r) = 1 - \left(\frac{1}{R_i} + \frac{1}{R_e}\right) r + \left(\frac{1}{R_i R_e}\right) r^2, \tag{A.4.a}$$

$$f_2(r) = \left(\frac{R_e}{R_i t}\right) r - \left(\frac{1}{R_i t}\right) r^2, \tag{A.4.b}$$

$$f_3(r) = -\left(\frac{R_i}{R_e t}\right) r + \left(\frac{1}{R_e t}\right) r^2, \tag{A.4.c}$$

being $t = R_e - R_i$ the thickness of the annular wall. It results:

$$\lim_{t\to 0} f_1 = 0, \qquad \lim_{t\to 0} f_2 = \frac{1}{2}, \qquad \lim_{t\to 0} f_3 = \frac{1}{2} \tag{A.5.a-c}$$

5.3. Strain and stress components

Due to the condition $u_\vartheta = 0$, the infinitesimal strain tensor assumes the following form:

$$\boldsymbol{\varepsilon} = \begin{bmatrix} \varepsilon_1 & 0 & \varepsilon_{13} \\ 0 & \varepsilon_2 & 0 \\ \varepsilon_{31} & 0 & \varepsilon_3 \end{bmatrix} \tag{A.6}$$

where:

$$\varepsilon_1 = \varepsilon_r = \frac{\partial u_r}{\partial r}, \qquad \varepsilon_2 = \varepsilon_\vartheta = \frac{u_r}{r}, \tag{A.7.a-b}$$

$$\varepsilon_3 = \varepsilon_z = \frac{\partial w}{\partial z}, \qquad \varepsilon_{13} = \varepsilon_{31} = \varepsilon_{rz} = \frac{1}{2}\left(\frac{\partial u_r}{\partial z} + \frac{\partial w}{\partial r}\right). \tag{A.7.c-d}$$

For orthotropic behaviour, it also results:

$$\begin{bmatrix} \varepsilon_r \\ \varepsilon_\vartheta \\ \varepsilon_z \\ \varepsilon_{rz} \end{bmatrix} = \begin{bmatrix} S_{11} & S_{12} & S_{13} & 0 \\ S_{21} & S_{22} & S_{23} & 0 \\ S_{31} & S_{32} & S_{33} & 0 \\ 0 & 0 & 0 & S_{44} \end{bmatrix} \begin{bmatrix} \sigma_r \\ \sigma_\vartheta \\ \sigma_z \\ \tau_{rz} \end{bmatrix}, \quad \begin{bmatrix} \sigma_r \\ \sigma_\vartheta \\ \sigma_z \\ \tau_{rz} \end{bmatrix} = \begin{bmatrix} C_{11} & C_{12} & C_{13} & 0 \\ C_{21} & C_{22} & C_{23} & 0 \\ C_{31} & C_{32} & C_{33} & 0 \\ 0 & 0 & 0 & C_{44} \end{bmatrix} \begin{bmatrix} \varepsilon_r \\ \varepsilon_\vartheta \\ \varepsilon_z \\ \varepsilon_{rz} \end{bmatrix} \tag{A.8.a-b}$$

where:

$$S_{11} = \frac{1}{E_T} \qquad S_{12} = -\frac{\nu_{TT}}{E_T} \qquad S_{13} = -\frac{\nu_{LT}}{E_L} \tag{A.9.a-c}$$

$$S_{21} = -\frac{\nu_{TT}}{E_T} \qquad S_{22} = \frac{1}{E_T} \qquad S_{23} = -\frac{\nu_{LT}}{E_L} \tag{A.9.d-f}$$

$$S_{31} = -\frac{\nu_{TL}}{E_T} \qquad S_{32} = -\frac{\nu_{TL}}{E_T} \qquad S_{33} = \frac{1}{E_L} \tag{A.9.g-i}$$

$$S_{44} = \frac{1}{2G_{TL}} \tag{A.9.j}$$

$$C_{11} = \frac{1-\nu_{TL}\nu_{LT}}{E_T E_L \Delta}, \qquad C_{12} = \frac{\nu_{TT}+\nu_{LT}\nu_{TL}}{E_T E_L \Delta} \qquad C_{13} = \frac{\nu_{LT}+\nu_{TT}\nu_{LT}}{E_T E_L \Delta} \tag{A.10.a-c}$$

$$C_{21} = \frac{\nu_{TT}+\nu_{LT}\nu_{TL}}{E_T E_L \Delta} \qquad C_{22} = \frac{1-\nu_{TL}\nu_{LT}}{E_T E_L \Delta} \qquad C_{23} = \frac{\nu_{LT}+\nu_{TT}\nu_{LT}}{E_T E_L \Delta} \tag{A.10.d-f}$$

$$C_{31} = \frac{\nu_{LT}+\nu_{TT}\nu_{LT}}{E_T E_L \Delta} \qquad C_{32} = \frac{\nu_{LT}+\nu_{TT}\nu_{LT}}{E_T E_L \Delta} \qquad C_{33} = \frac{1-\nu_{TT}\nu_{TT}}{E_T E_T \Delta} \tag{A.10.g-i}$$

$$C_{44} = 2G_{TL} \tag{A.10.j}$$

with $\frac{\nu_{LT}}{E_L} = \frac{\nu_{TL}}{E_T}$, $\Delta = \frac{1-\nu_{TT}\nu_{TT}-2\nu_{TL}\nu_{LT}-2\nu_{TT}\nu_{TL}\nu_{LT}}{E_T E_T E_L}$, while $\mathbf{C} = \mathbf{S}^{-1}$. Moreover, the symbols "L" and "T" denote the axial and transverse directions.

5.4. Radial displacements

By appropriate steps:

$$\frac{\partial u_r}{\partial r} + a\frac{u_r}{r} + b w_i' f_i = 0 \tag{A.11}$$

where the symbol (.)' denotes the partial derivative with respect to z and the symbols “a” and “b” denote the following quantities:

$$a = \left(S_{1i}C_{i2}\right)/\left(1-S_{1i}C_{i1}\right) \qquad b = \left(S_{1i}C_{i3}\right)/\left(1-S_{1i}C_{i1}\right) \tag{A.13.a-b}$$

In eqs. (A.13) the Einstein summation has been considered.

It is worth noting that for thin or moderately thick wall annular cross-section, the assumption $\sigma_r \cong 0 \;\; \forall r \in \left[R_i, R_e\right]$ can be accepted if both the inner and the outer lateral surface are free of forces. This allows to specialize the values of a and b:

$$a = \frac{\nu_{TT} + \nu_{TL}\nu_{LT}}{1-\nu_{TL}\nu_{LT}} \qquad b = \frac{\nu_{LT} + \nu_{TT}\nu_{LT}}{1-\nu_{TL}\nu_{LT}} \tag{A.14.a-b}$$

A solution of eqn. (A.11) is searched according to the following form:

$$u_r(r,z) = \mathrm{q_i} w_\mathrm{i}(z) r^{-a} + w_\mathrm{i}'(z) g_\mathrm{i}(r) \tag{A.15}$$

where $\mathrm{q_i} = 1$ while $g_\mathrm{i}(r)$ (i=1, 2 , 3) are still unspecified functions of r.

Now eqn. (A.11) can be rewritten accounting for eqn. (A.15), thus giving:

$$w_\mathrm{i}'(z)\left[\frac{dg_\mathrm{i}(r)}{dr} + a\frac{g_\mathrm{i}(r)}{r} + bf_\mathrm{i}(r)\right] = 0 \tag{A.16}$$

By integrating the first order ordinary differential equations $\frac{dg_\mathrm{i}(r)}{dr} + a\frac{g_\mathrm{i}(r)}{r} + bf_\mathrm{i}(r) = 0$ (i=1, 2, 3), the final expressions of $g_\mathrm{i}(r)$ are obtained:

$$g_\mathrm{i}(r) = \frac{1}{r^a}\left[c_\mathrm{i} - b\int f_\mathrm{i}(r) r^a dr\right] \tag{A.17}$$

with c_i (i=1, 2, 3) to be determined by means of appropriate boundary conditions, as discussed in [13].

5.5. Explicit strain components

From eqs. (A.7.a-d), considering eqn. (A.2) and eqn. (A.15), it is easy to obtain the explicit form of the local strains ($a \neq 0$):

$$\varepsilon_r = \mathrm{q_i} w_\mathrm{i}(z) r^{-(a+1)} + w_\mathrm{i}'(z)\frac{\partial g_\mathrm{i}(r)}{\partial r}, \qquad \varepsilon_\vartheta = \mathrm{q_i} w_\mathrm{i}(z) r^{-(a+1)} + w_\mathrm{i}'(z)\frac{g_\mathrm{i}(r)}{r}, \tag{A.18.a-b}$$

$$\varepsilon_z = w_\mathrm{i}'(z) f_\mathrm{i}(r), \qquad \varepsilon_{rz} = \frac{1}{2}\left(\mathrm{q_i} w_\mathrm{i}'(z) r^{-a} + w_\mathrm{i}''(z) g_\mathrm{i}(r) + w_\mathrm{i}(z)\frac{\partial f_\mathrm{i}(r)}{\partial r}\right) \tag{A.18.c-d}$$

If $a = 0$, then eqn. (A.15) becomes

$$u_r(r,z) = \mathrm{q_i} w_\mathrm{i}(z) + w_\mathrm{i}'(z) g_\mathrm{i}(r) \tag{A.19}$$

As a consequence, eqs. (A.18.a-d) are replaced by:

$$\varepsilon_r = -b w_\mathrm{i}'(z) f_\mathrm{i}(r) \qquad \varepsilon_\vartheta = \mathrm{q_i} w_\mathrm{i}(z)\frac{1}{r} + w_\mathrm{i}'(z)\frac{g_\mathrm{i}(r)}{r} \tag{A.20.a-b}$$

$$\varepsilon_z = w_{\mathrm{i}}'(z)\, f_{\mathrm{i}}(r) \qquad \varepsilon_{rz} = \frac{1}{2}\left(\mathrm{q}_{\mathrm{i}} w_{\mathrm{i}}'(z) + w_{\mathrm{i}}''(z) g_{\mathrm{i}}(r) + w_{\mathrm{i}}(z) \frac{\partial f_{\mathrm{i}}(r)}{\partial r} \right) \quad \text{(A.20.c-d)}$$

If $a = 0$ and $b = 0$, eqn. (A11) indicates that u_r does not depend on the radial coordinate r. Considering the condition:

$$\lim_{r \to 0} u_r = 0 \tag{A.21}$$

it results:

$$u_r = 0 \tag{A.22}$$

Finally:

$$\varepsilon_r = 0 \qquad \varepsilon_{\vartheta} = 0 \qquad \text{(A.23.a-b)}$$

$$\varepsilon_z = w_{\mathrm{i}}'(z)\, f_{\mathrm{i}}(r) \qquad \varepsilon_{rz} = \frac{1}{2}\left(w_{\mathrm{i}}(z) \frac{\partial f_{\mathrm{i}}(r)}{\partial r} \right) \qquad \text{(A.23.c-d)}$$

More in detail, eqn. (A.23.d) indicates that the shear strain ε_{rz} is a linear function of r. This last simplification has been considered with reference to the numerical example presented in Section 3.

REFERENCES

[1] M.S. Kafkalidis, M.D. Thouless, The effects of geometry and material properties on the fracture of single lap-shear joints. *International Journal of Solids and Structures*, **31**, 2537-2563, 2002.

[2] A.T. Abdelaziz, R. Boukhili, S. Achiou, S. Gordon, H. Boukehili, Bonded joints with composite adherends. Part I. Effect of specimen configuration, adhesive thickness, spew fillet and adherent stiffness on fracture. *International Journal of Adhesion and Adhesives*, **26**, 226-236, 2006.

[3] A.T. Abdelaziz, R. Boukhili, S. Achiou, H. Boukehili, Bonded joints with composite adherents. Part II. Finite element analysis of joggle lap joints. *International Journal of Adhesion and Adhesives*, **26**, 237-248, 2006.

[4] L.F.M. da Silva, R.D. Adams, Joint strength predictions for adhesive joints to be used over a wide temperature range. *International Journal of Adhesion and Adhesives*, **27**, 362-379, 2007.

[5] F. Ascione, G. Mancusi, Axial/Bending coupled analysis for FRP adhesive joints. *Mechanics of Advanced Materials and Structures*, **17**, 1–14, 2010.

[6] F. Ascione, G. Mancusi, Failure criteria for FRP adhesive lap joints: a comparative anal ysis. *Mechanics of Advanced Materials and Structures*, **17**,157–164, 2010.

[7] G. Mancusi, F .Ascione, Performance at collapse of adhesive bonding. *Composite Structures*, **96** ,256–261, 2013.

[8] L. Ascione, L. Feo, G. Mancusi, On the statical behaviour of fibre-reinforced polymer thin-walled beams, *Composites Part B: Engineering*, **31** (8), 643-654, 2000.

[9] L. Feo, G. Mancusi, Modeling shear deformability of thin-walled composite beams with open cross-section, *Mechanics Research Communications*, **37** (3), 320-325, 2010.

[10] L. Feo, G. Mancusi, The influence of the shear deformations on the local stress state of pultruded composite profiles. *Mechanics Research Communications* **47,** 44– 49, 2013.

[11] J.H. Rose, J. Ferrante, J.R. Smith, Universal binding energy curves for metals and bimetallic interfaces. *Physical Review Letter*, **47**, 675–678, 1981.

[12] J.H. Rose, J.R. Smith, J. Ferrante, Universal features of bonding in metals. *Physical Review B*, **28**,1835–1845, 1983.

[13] G. Mancusi, Elastic Behaviour of Thick-Walled Composite Tubes. Submitted to *Composite Structures*.

[14] F. Fraternali, Free Discontinuity Finite Element Models in Two-Dimensions for In-Plane Crack Problems. *Theoretichal and applied fracture mechanics*, **47**, 274-282, 2007.

[15] F. Fraternali, M. Negri, M. Ortiz, On the convergence of 3D free discontinuity models in variational fracture. *International Journal of Fracture*, **166** (1-2), 3-11, 2010.

[16] M. Angelillo, E. Babilio, A. Fortunato, Numerical solutions for crack growth based on the variational theory of fracture. *Computational Mechanics*, **50** (3), 285-301, 2012.

[17] G. Carpentieri, M. Modano, F. Fabbrocino, F. Fraternali, Optimal design and dynamics of truss bridges. *5th Thematic Conference on Computational Methods in Structural Dynamics and Earthquake Engineering (COMPDYN-ECCOMAS2015)*, 1731-1740, 2015.

[18] G. Carpentieri, R.E. Skelton, F. Fraternali, Minimum mass and optimal complexity of planar tensegrity bridges. *International Journal of Space Structures*, **30** (3-4), 221-243, 2015.

[19] R.E. Skelton, F. Fraternali, G. Carpentieri, A. Micheletti, Minimum mass design of tensegrity bridges with parametric architecture and multiscale complexity. *Mechanics Research Communications*, **5**8, 124-132, 2014.